Lawrence Berkeley National Laboratory

Title
Hybrid Composite Coatings for Durable and Efficient Solar Hydrogen Generation under Diverse Operating Conditions

Permalink
https://escholarship.org/uc/item/7n4466gs

Journal
Advanced Energy Materials, 7(13)

ISSN
1614-6832

Authors
Walczak, Karl A
Segev, Gideon
Larson, David M
et al.

Publication Date
2017-07-01

DOI
10.1002/aenm.201602791

Peer reviewed

Hybrid Composite Coatings for Durable and Efficient Solar Hydrogen Generation Under Diverse Operating Conditions

Karl A. Walczak, Gideon Segev, David M. Larson, Jeffrey W. Beeman, Frances A. Houle, Ian D. Sharp*

Dr. K.A. Walczak, Dr. G. Segev, D.M. Larson, J.W. Beeman, Dr. F.A. Houle, Dr. I.D. Sharp
Chemical Sciences Division and Joint Center for Artificial Photosynthesis
Lawrence Berkeley National Laboratory
Berkeley, CA 94720 USA
E-mail: idsharp@lbl.gov

Safe and practical solar-driven hydrogen generators must be capable of efficient and stable operation under diurnal cycling with full separation of gaseous H_2 and O_2 products. Here, a novel architecture that fulfills all of these requirements is presented. The approach is inherently scalable and provides versatility for operation under diverse electrolyte and lighting conditions. The concept is validated using a 1 cm^2 triple-junction photovoltaic cell with its illuminated photocathode protected by a composite coating comprising an organic encapsulant with an embedded catalytic support. The device is compatible with operation under conditions ranging from 1 M H_2SO_4 to 1 M KOH, enabling flexibility in selection of semiconductor, electrolyte, membrane, and catalyst. Stable operation at a solar-to-hydrogen conversion efficiency of >10% is demonstrated under continuous operation, as well as under diurnal light cycling for at least four days, with simulated sunlight. Operational characteristics are validated by extended time outdoor testing. A membrane ensures products are separated, with non-explosive gas streams generated for both alkaline and acidic systems. Analysis of operational characteristics under different lighting conditions is enabled by comparison of a device model to experimental data.

1. Introduction

Since the first demonstration of photoelectrochemical water splitting,[1] significant progress has been made in demonstrating high-efficiency, solar-driven hydrogen generators using various architectures and materials combinations, as summarized in a recent review article.[2] Additional demonstrations, published since the time of that review, have incorporated novel materials, designs, and corrosion protection schemes.[3-5] While energy conversion efficiency is an important characteristic of such devices,[6] recent prospective lifecycle assessments[7, 8] and technoeconomic analyses[9] have highlighted that device lifetime is also a critical consideration for a viable technology. Efficiency is affected by the combinations of materials used, the operational electrochemical environment, and the physical arrangement of the components within the device. Lifetime is affected by the stability of materials during active and inactive periods in contact with electrolyte, which are defined by photoelectrochemical and electrochemical properties of the materials, respectively, as well as the presence of defects over various length scales. In addition, safe operation requires separation of hydrogen and oxygen products to ensure explosive gas mixtures are not generated at any location in the device.[10] Simultaneously achieving high efficiency, long lifetime, and pure gas product streams is the key challenge to realizing useful device performance characteristics.

As discussed in numerous publications,[10, 11] steady state solar-to-hydrogen (STH) conversion efficiency is increased by operation of solar water splitting devices under extreme pH conditions. Relative to near-neutral pH, acidic or alkaline conditions minimize catalytic overpotential requirements and mass transport limitations to the electrode surface, thereby leading to reduced solution resistance (*IR*) losses and pH swings at electrode surfaces. However, the majority of semiconductor light absorber materials that have bandgaps in the optimum range for harvesting sunlight are not

stable under these conditions.[12] Such chemically sensitive materials can be protected by introduction of optically transparent, electrically conducting, and chemically inert layers at the semiconductor/electrolyte interface.[13] These conformal thin films are typically grown by techniques such as atomic layer deposition (ALD), physical vapor deposition (PVD), or photoelectrochemical self-passivation,[3] followed by growth of a catalyst layer.[13] Alternatively, the catalyst can itself serve as the protection layer, such as for the case of thin films of NiO_x[14] or CoO_x.[15] Regardless of approach, these layers stabilize the efficiency and increase the lifetime of the photoelectrode, while minimizing optical, electrical, and catalytic losses. In practice, the creation of semiconductor/protection layer/catalyst assemblies, with each material and interface possessing optimized chemical and electronic properties and having no defects through which the electrolyte can penetrate, remains a critical challenge.

Corrosion protection layers have recently been applied to devices capable of light-driven overall water splitting with no external applied bias. For example, high-efficiency tandem III-V semiconductor devices, with illuminated photoanode and dark cathode, were stabilized by ALD of TiO_2 on the surface of the photoanode.[4] These devices included membranes for product separation and exhibited lifetimes as long as 80 h, but with steadily declining efficiencies beyond approximately 24 h. The stringent requirement for no defects in the protection layer restricted the total photoelectrode surface area to less than 1 mm^2.[4] Operation of a similar device using the same semiconductor stack and a bipolar membrane, with the photoanode exposed to near-neutral pH electrolyte and dark cathode exposed to pH 0 acid, yielded long lifetimes with larger surface areas. However, the use of bipolar membranes introduces a separate set of challenges for optimized device design, intermittent operation, and scale-up.[5, 16] In another example, May *et al.*[3] developed an *in situ* photocathode passivation method that was applied to a tandem III-V cell in a configuration with no membrane to

3

achieve a STH efficiency of 14%. This method improves stability via elegant control of the semiconductor/electrolyte interface, but introduces some complexity for subsequent incorporation of the reduction reaction catalyst.[3] Moreover, many useful semiconductor electrode materials cannot self-passivate,[17] so the utility of this approach is limited to select semiconductor compositions. A summary of prior reports of III-V semiconductor-based solar water splitting devices, including those that are directly integrated with catalyst and those that are wired to electrolysis devices, is presented in Table S1.

The value of ALD as a protective coating method is that it is conformal and, when process conditions favor dense, uniform surface coverages, leads to high-quality films. In practice, such conditions are difficult to achieve, particularly as device dimensions are increased. On the other hand, organic thin films with *in situ* crosslinking can form transparent, dense, and conformal coatings that are stable in the presence of acid or base. If provided with conducting pathways to connect the semiconductor to the catalyst, such protection layers offer an alternative for semiconductor systems that do not require a liquid junction, cannot self-passivate, and are readily corroded. In this work, we demonstrate the utility of this alternative protection system for spontaneous, solar-driven water splitting devices. Rather than depositing inorganic thin-film passivation layers and placing oxidation or reduction catalysts on them, we show that placing a catalyst on a conducting grid support in intimate contact with the top surface of the bare electrode and embedding the assembly in a transparent polymer leads to both high efficiency and long lifetimes. This new architecture protects the photovoltaic (PV) from the harsh aqueous electrolyte operating environment, and allows direct charge transfer from the PV to the catalyst in contact with the liquid for efficient conversion of visible light to H_2 and O_2. We show that this method offers a number of advantages, including operation at both pH 0 and pH 14, as well as stability with

respect to diurnal cycling and operation outdoors. Most importantly, this approach provides great flexibility in the selection of materials and their processing conditions since the device components are prepared separately and integrated as a final step. This assembly is demonstrated to operate routinely for spontaneous light-driven water splitting at a STH efficiency of >10% over days, with significant opportunity for further optimization, particularly with respect to the PV element. The simplicity of the fabrication method offers a potentially highly manufacturable path for practical large-scale solar fuels devices.

2. Results

2.1. Construction of a Composite-Protected Solar Hydrogen Device

A schematic of the process steps used to fabricate an efficient and stable solar hydrogen device is shown in **Figure 1a**. Since the focus of this work is on development of a new approach to protecting the semiconductor light absorber, without need for energy-, material-, and time-intensive processes, we chose to use a commercially available multi-junction PV element as the core of the device. In particular, we selected the Ultra Triple Junction (UTJ) PV cell from Spectrolab, Inc., which provides a suitable platform for characterizing stability and, as described below, possesses illuminated current-voltage characteristics that could allow for STH efficiencies of >10% in a monolithic assembly.[18] The architecture of the PV, which is based on a Ge bottom cell, GaAs middle cell, and InGaP top cell, drives photo-generated electrons to the illuminated front surface and holes to the back surface.[18] For solar-driven water splitting, this dictates that H_2 will be produced on the illuminated cathode and O_2 will be produced on the backside anode.

The triple junction PV cells were diced into 1×1 cm^2 pieces and mounted into an acrylic chassis. The composite coating, which protects the PV element, allows charge transport, and provides catalytic activity, was fabricated on the surface of the mounted

triple junction cell. A Pt-coated Ti mesh, which provides both electrical conductivity and activity for the hydrogen evolution reaction (HER), was compressed against the surface of the PV cell. This mesh was then infilled by a novolac phenol-formaldehyde resin, which was selected as an optically transparent and chemically resistant epoxy (Epotek 302-3M), and was then degassed and cured, as described in the Methods section. Because there is no chemical bonding between the catalyst-coated mesh and the PV element, intimate physical contact between the two was maintained during curing of the epoxy by mechanically pressing the grid onto the light absorber. This ensured good electrical contact between components. High efficiency charge extraction from the PV was promoted by the presence of metallic strip contacts on the commercial devices. This efficiency is expected to be similar for other PV devices with doped top surface window layers or transparent conductive layers. For the present study, a Pt coating was selected as the HER catalyst because of its high activity and chemical stability at both high and low pH. We note that other catalysts could be integrated using the same approach; the primary requirement would be good adhesion between the catalyst and the electrically conductive mesh.

Figure 1b shows a cross-sectional illustration of the grid/epoxy composite-coated photovoltaic element. The epoxy physically separates the chemically sensitive semiconductor stack from the harsh aqueous environment required for photoelectrolysis. The grid used in this work is woven from metallic wires and the resulting three-dimensional structure is beneficial for ensuring complete infilling of epoxy. Furthermore, this structure promotes protrusion of the catalyst-coated metallic grid above the surface of the epoxy to ensure formation of an interface between the catalyst and the electrolyte. A plan-view optical micrograph of the assembly is shown in **Figure 1c**.

Since the photovoltaic element is illuminated through the composite coating, the optical properties of the epoxy and form factor of catalyst-coated grid have a direct impact on efficiency. As shown in **Figure 2a** the Epotek 302-3M epoxy is characterized by high optical transmission across the visible spectral range and to wavelengths beyond the Ge bandgap in the infrared. This low optical loss, combined with chemical stability from low to high pH, makes this material well suited as a protective encapsulant in solar fuels devices. However, the Ti grid partially shadows the photovoltaic element. In the present study, commercially available Ti wire grids that are 67.4% transmissive were used. The optical loss can be minimized by optimization of the three dimensional grid structure, providing an opportunity for significant improvement of STH efficiency.

Solid state photocurrent density versus applied voltage (*JV*) curves were collected in order to understand the impact of the composite coating on the photovoltaic properties of the triple junction cell. The Spectrolab UTJ cell used in this work was designed for non-terrestrial applications. The constituent bandgaps and anti-reflection coatings are optimized for AM 0 irradiation at 1350 W m^{-2}, under which conditions the manufacturer-specified open circuit voltage (V_{oc}) and short circuit current density (J_{sc}) are 2.66 V and 17.05 mA cm^{-2}, respectively.[19] As shown in **Figure 2b**, under simulated AM1.5G light at 1000 W m^{-2}, we measure V_{oc}, J_{sc}, and fill factor (FF) to be 2.55 V, 14.85 mA cm^{-2}, and 0.70, respectively, which correspond to a power conversion efficiency (PCE) of 26.4%. Application of the composite coating introduces optical losses that reduce these values to 2.47 V, 9.72 mA cm^{-2}, and 0.70, respectively. The resulting solid state PCE, with the composite coating in place and under simulated 1 Sun illumination, is thus 16.85%.

To better forecast the operational points of assembled solar water splitting devices based on composite-protected triple junction cells, the solid state *JV* characteristics from the

photovoltaic were compared to three-electrode current density versus applied electrochemical potential (*JE*) measurements of the HER and oxygen evolution reaction (OER) catalysts in different electrolytes, as shown in Figure 2b. Under both acidic (1 M H_2SO_4, pH = 0) and alkaline (1 M KOH, pH = 13.7) conditions, the encapsulated Pt-coated Ti mesh was used as HER catalyst. For OER under the same acidic and alkaline conditions, IrO_x and $NiFeO_x$ catalysts, respectively, were used. Inspection of the photovoltaic and electrochemical characteristics reveals that triple junction cell should provide sufficient voltage to drive the overall water splitting reaction with no external bias at current densities corresponding to STH conversion efficiencies greater than 10% in both acid and base.

2.2. Functional Characteristics of Protected Water Splitting Cells

Figure 3 shows an illustration of the custom cell used to characterize performance of fully assembled devices for unbiased photo-driven water splitting. Cell design was guided by modelling and simulation to minimize *IR* losses in solution, while allowing for product separation with ion-conducting membranes.[20] The chassis was machined from acrylic, which provides good stability under both acidic and alkaline testing conditions. A summary of the material components used in different electrolytes is provided in **Table 1**. Although the OER catalysts could be monolithically integrated into the device, as illustrated in Figure 1a, such a configuration prohibits measurement of the electrical current in the system. Therefore, we characterized performance in the modified geometry shown in Figure 3, in which the OER catalyst was deposited onto a conductive support that was wired to the backside of the photovoltaic stack. Separation of O_2 and H_2 products, which is essential for ensuring no explosive gas mixtures are present within the system and for reducing product back reaction and crossover losses, was achieved using a proton conducting membrane (Nafion XL-100) in acid and an anion conducting membrane (AHA Neosepta) in base.

The two-electrode cyclic voltammetric behavior of fully assembled devices in both acidic and alkaline conditions is shown in **Figure 4a**. The measurements were conducted with membranes separating the photocathode and anode compartments, so all internal cell *IR* losses are accounted for in these measurements. The exact same photocathode was used in both electrolytes, and only membranes, OER catalysts, and electrolyte were changed between the acquisitions of voltammograms. The two-electrode performance is in good agreement with prediction based on the solid-state characterization presented in Figure 2b. However, the saturation current density is lower, likely because of optical losses from water, as described below.

The stabilities of the light-driven water splitting devices in acid and base were evaluated by chronoamperometric measurements with no applied electrical bias and no external mixing, as shown in **Figure 4b**. In both cases, the device was found to be stable for at least 10 h of sustained operation and, as will be discussed below, stability extended to much longer times. Using these data for the photocurrent density in the absence of applied external bias, the STH conversion efficiency, η, was calculated according to the standard expression:[2]

$$\eta = \frac{(1.23 \text{ V})(J_{op})}{P_{in}} \tag{1}$$

where 1.23 V is the thermodynamic potential for water splitting, J_{op} is the operational photocurrent density in mA cm^{-2}, and P_{in} is the incident irradiance in mW cm^{-2}. The STH conversion efficiencies, provided on the right vertical axis of Figure 4b, were greater than 10% during both experiments. These results were typical, with measurement of 10 independent devices yielding steady state STH conversion efficiencies between 8% and 12.5%. The major source of variation is likely edge shunts from dicing of commercial Spectrolabs UTJ material into 1×1 cm^2 chips.

Comparison of the curves in Figure 4b reveals that there is more variation around the mean of photocurrent density during illuminated operation under acidic conditions than under basic conditions. Importantly, this variability is not due to noise; it is a consequence of bubble accumulation and release from the illuminated surface of the electrodes. As can be seen in the videos included in the Supporting Information, H_2 bubbles produced in the 1 M KOH electrolyte appeared to be smaller and released more quickly than in 1 M H_2SO_4. This observation suggests that careful consideration and control over interface energies is important for mitigating the effect of bubbles on the time-integrated H_2 production rate and overall device performance.

The Faradaic efficiency, purity of products, and gas crossover were evaluated by analyzing the H_2 and O_2 generated in 1 M H_2SO_4 and 1 M KOH electrolytes using gas chromatography (GC). The device and GC were connected inline such that product gases from the anode and cathode chambers could be analyzed separately, as described in the Methods section. All values are given as absolute measurements, without compensation for gas leaks, diffusion through the acrylic cell or tubing, or for dissolved species in the electrolyte. The results, provided in **Table 2**, indicate a Faradaic efficiency for H_2 production near 100%. The GC-measured H_2 production rates correspond to STH efficiencies of 10.54% and 10.90% for operation in 1 M H_2SO_4 and 1 M KOH, respectively. We note that the ratio of H_2:O_2 deviated from 2.0, with the acidic and alkaline conditions yielding ratios of 2.38 and 2.17. This variation is likely due to accumulation of trapped oxygen bubbled in the anode chamber, which were observed during all experiments. Under acidic and alkaline conditions, the concentrations of H_2 measured in the O_2 streams were 0.94% and 1.37%, respectively. In addition, the corresponding concentrations of O_2 measured in the H_2 streams were 0.37% and 0.12%. Thus, non-explosive gas mixtures are produced for all device configurations.

2.3. Performance and Stability Analysis Under Diurnal Cycling

Although the stability and efficiency of nearly all solar hydrogen generators are tested under continuous illumination,[21] real systems must operate under solar insolation that varies continuously in intensity and spectral distribution throughout the day and year. Therefore, device materials must be physically and chemically robust during illuminated operation and under extended periods of rest in the dark. Repeated temperature cycling and non-steady state pH gradients within devices have potential to introduce failures that would not be predicted by continuous illumination tests alone. In order to explore whether performance is recovered day after day, stability was assessed under diurnal cycling. To this end, two exploratory studies were performed: one under simulated diurnal cycling in the laboratory and the other outdoors in real sunlight.

Chronoamperometric testing under simulated diurnal cycling was carried out over a period of 7 days, alternating between 12 h of steady AM 1.5G light at 100 mW cm^{-2} and 12 h in darkness, all under acidic conditions. Photocurrent density and STH conversion efficiency as a function of time are shown in **Figure 5**, together with measurements of the changes of light intensity and temperature that were acquired with a photovoltaic Si reference cell with integrated thermocouple (see Methods section for details). During the first 4 days, the illuminated photocurrent density was stable and, after repeated 12 h dark cycling, rapidly recovered steady state operation at a STH conversion efficiency of approximately 10%.

The production rate and purity of gasses generated during the illuminated period of Day 4 were analyzed with inline gas chromatography (GC), as described in the Methods section. The GC-measured H_2 production rate corresponded to a STH conversion efficiency of $10.55 \pm 0.57\%$, where the uncertainty is given by the standard deviation over 10 sample intervals. This value is in excellent agreement with the electrically measured STH conversion efficiency above 10%. The crossover losses are

11

similar to those presented above, indicating that there is little degradation of the Nafion membrane during 4 days of testing with simulated diurnal cycling.

Although stable operation was observed through Day 4, the STH conversion efficiency declined from 10% to 9% from Day 5 to Day 7. Unlike the precipitous catastrophic failure that is characteristic of chemical attack of the photovoltaic element (see **Figure S1**), this performance degradation was gradual and incomplete. In order to identify the source of degradation, the samples were inspected by optical and scanning electron microscopy. No evidence for failure of the composite coating or chemical attack of the underlying semiconductor was found. However, elemental analysis of the Pt-coated Ti grid in electrolyte-exposed regions revealed delamination of the Pt HER catalyst from the metallic support (**Figure S2**). This indicates that engineering of the catalyst/metal support interface can provide a route to improved long-term stability, which is a topic of future research. Historically, failure of efficient water splitting devices has been dominated by corrosion of the semiconductor light absorber.[2] The development of an effective semiconductor protection strategy, such as that reported here, provides an opportunity to explore a new regime, in which the next set of longer term failure modes become apparent.

In addition to simulated diurnal light cycling in the laboratory, outdoor testing of a complete device assembly was performed over a 30 h period on the roof of Chu Hall, which houses the Joint Center for Artificial Photosynthesis, at Lawrence Berkeley National Laboratory. The testing apparatus consisted of a custom two-axis solar tracker, a potentiostat for collecting photocurrent as a function of time with no applied bias, a calibrated reference Si photovoltaic cell for monitoring light intensity, a thermocouple for collecting the temperature of the reference cell, and a video camera, as shown in the photograph in **Figure S3**. **Figure 6** shows the resulting chronoamperometric data from the composite-protected solar water splitting cell, together with the incident light intensity and temperature from the reference photovoltaic cell.

Considerable incident light intensity and temperature fluctuations were observed, as expected under outdoor testing conditions. Under full illumination near mid-day, the photocurrent density from the solar water splitting cell was greater than 8 mA cm^{-2}, both on the first and second day. This reproducible current density is consistent with the stable operational characteristics determined from lab-based experimentation. As described in the next section, the photocurrent density and light intensity did not track one another linearly, which points to a need to more fully address the device physics.

2.4. Operational Principles of Protected Triple Junction Water Splitting Cells

Theoretical efficiency analyses of photo-driven water splitting cells have frequently assumed that AM1.5G spectral illumination is incident on the semiconductor light absorber. However, Döscher and co-workers recently pointed out that optical absorption in the electrolyte, through which light must pass in most monolithically integrated solar water splitting device architectures, significantly reduces intensity in the infrared spectral region.[22] This important observation has significant implications for the functional characteristics of devices based on multi-junction photovoltaic elements, and especially for triple junction cells such as the one reported here. The Spectrolab UTJ cell comprises a InGaP top cell (E_g ~2.0 eV), a GaAs middle cell (E_g =1.424 eV), and a Ge bottom cell (E_g = 0.67 eV). Under full spectrum solar irradiation, this architecture leads to excess photogenerated current density in the Ge bottom cell due to absorption of infrared light. In a monolithically integrated water splitting device, however, the majority of the infrared light is absorbed by the aqueous electrolyte.[22] In this case, the Ge bottom cell may limit the current in the top and middle cells, which are electrically in series, and would therefore limit maximum achievable efficiency. While the bottom cell could receive a small boost through luminescent coupling, in which emitted photons from the top and middle cells are absorbed by the bottom

cell,[23] this effect would be small since the external quantum efficiencies of the top and middle cells are ~90%, as reported by the manufacturer.

In order to understand the effect of infrared light absorption by water on the performance characteristics of the triple junction photovoltaic element, *JV* curves of diced UTJ solar cells were measured when illuminated through 10 mm and 20 mm thick water filters, resulting in spectral changes presented in **Figure 7a**. **Figure 7b** shows the resulting *JV* curves obtained with and without the water filters. The shapes of the *JV* curves obtained under filtered illumination deviate significantly from the unfiltered case, as well as from model expectations. The inset of Figure 7b shows the predicted *JV* characteristic obtained using an equivalent circuit model consisting of three single diode sub-cells connected in series, with each representing one junction in the photovoltaic cell (see Supporting Information for details of device model).[24] For the current mismatched triple-junction cell operated under water-filtered illumination, the basic shape of the *JV* curve is predicted to be similar to that obtained under unfiltered illumination, but with a significant reduction of the short circuit current and small decrease of the open circuit voltage. In contrast, the measured curves exhibit an unanticipated inflection point between short circuit and the open circuit voltage, as well as a significantly larger short circuit current density than predicted.

The "double knee" shape of the *JV* characteristics presented in Figure 7b is consistent with Ge junction breakdown due to reverse biasing by the other two junctions.[25] In such a case, the photovoltage produced by the InGaP top and GaAs middle junctions, which can be larger than 2 V, applies a negative bias on the Ge junction resulting in avalanche breakdown at low voltages. As a result, the short-circuit current is determined by photon absorption in the top and middle junctions instead of being restricted to the photo-limited Ge current. This mechanism would increase the current density at the operating point, which is given by the intersection of the *JV*

curve with the electrochemical load curve. The breakdown characteristics may also be enhanced by defects introduced during the dicing process. At voltages near the open circuit voltage, the total current density through the cell is lower than the photo-limited current density of the Ge junction so that this junction no longer limits the output.

To describe the water-filtered *JV* characteristics, an avalanche breakdown term was added to the Ge junction sub-cell of the equivalent circuit device model.[25] An elaborated description of the model and its calibration can be found in the Supporting Information. **Figure 8a-c** show the measured and modeled *JV* curves obtained with simulated AM1.5G illumination intensities between 0.1 sun and 1 sun passing through no filter, the 10 mm water filter, and the 20 mm water filter, respectively. Excellent agreement between experimental observations and the device model, with Ge junction breakdown, is obtained for all lighting conditions. The thick dashed line is the experimental electrochemical load curve for the combined Pt HER and NiFeO$_x$ OER catalyst, obtained from the data in Figure 2b. Its intersection with the illuminated *JV* curves gives the device operating point. The potential STH conversion efficiency of the cells can be estimated by inserting the operating point current density into **Equation 1**. Breakdown of the Ge junction allows more current to flow through the cell near the operating point, thereby slightly compensating for the current mismatch losses inflicted by infrared light absorption by the water. It should also be noted that at low light intensities the current mismatch is less severe. As a result, optical filtering by water has a smaller impact on device performance, which leads to higher STH conversion efficiencies at lower illumination intensities, as observed experimentally.

Figure 8d shows the simulated behavior of a solar cell consisting only of the UTJ middle and top junctions illuminated through 10 mm of water. Since this cell does not absorb in the IR, its performance is not limited by current mismatches arising from light absorption in water. Comparison of the predicted *JV* characteristics of this

hypothetical tandem junction device, which itself is not optimized to the incident spectrum, to those of the experimentally used triple junction device highlights a considerable opportunity for increasing STH conversion efficiency at all but the lowest light intensities.

Figure 9 shows the STH conversion efficiency as a function of the light intensity extracted from the outdoor testing experiments described above, along with those calculated for the triple junction cell with 10 mm and 20 mm water filters, accounting for reduced transmission through the composite coating, as well as the hypothetical dual junction device. As discussed above, reduced current mismatch losses lead to higher STH conversion efficiencies at low light intensities. It should be noted that, during outdoor testing, the incident sunlight power density was measured using a calibrated Si reference cell (Newport 91150V), with an operational range of 0 to 3.5 suns, absorbing light in the range of 350 to 1100 nm with peak absorbance at 970 nm. This measurement does not accurately account for changes of the solar spectrum during the day. As has been pointed out,[22] spectral mismatch between detector sensitivity and the AM1.5G solar simulator irradiance can cause significant error in the calculated STH conversion efficiency. The scatter in our outdoor testing results suggest that this is also a consideration for measurements in natural sunlight where the season, angle of incidence, clouds, fog, air pollution, and altitude can significantly change the irradiance and spectrum, and subsequently the accuracy of the calculated STH conversion efficiency. This is especially true in low light, whether seasonal or at the beginning and end of each day, where small changes in the spectral distribution can significantly impact the accuracy of measured irradiance because the underlying assumption in the measurement is that the spectral distribution is not changing. Just as best practices are being established for indoor efficiency testing[26] a similar set of protocols needs to be established for outdoor testing.

3. Discussion

Although the assembled devices reported here were characterized by high STH efficiency exceeding 10% and long-term durability under reaction conditions, this work also revealed a number of aspects of this architecture that can be improved. They fall into three main groups: light management, interfacial stability, and bubble management.

The fraction and wavelength distribution of incident light that is absorbed by the photovoltaic element is primarily controlled by: (i) the chemical composition of the epoxy, (ii) thickness of the epoxy, (iii) the reflectivity at the epoxy/PV and epoxy/electrolyte interfaces, (iv) the transparency of the mesh support, and (v) the detailed structure and compositions of the photovoltaic device, including the semiconductor materials stack, anti-reflection coatings, and contact layers. As shown in Figure 2a, transmission through the epoxy is high across the range of wavelengths absorbed by the triple junction device. However, the Ti mesh blocks over 30% of incident light across all wavelengths, indicating that efficiency could be significantly improved by use of a fine gauge mesh. While this would complicate incorporation of the polymer to form a continuous composite, it is likely that a satisfactory fabrication method can be devised. In addition, it is possible that long-term stability of the epoxy in illuminated and reactive environments may affect its transparency. Increasing opacity was not observed in the present work. However, operation times were short compared to those expected for the energy return of a practical system to be positive[7] and yellowing or other changes that are typical of polymer degradation could occur over time. Possible (photo)chemical routes to epoxy degradation must be identified and development of photo-stable compositions specifically engineered for application in artificial photosystems may be necessary.

Optimization of the photovoltaic element provides considerable opportunity for more efficient light harvesting and conversion to chemical product. In the present

work, the goal was to use established and commercially available components in order to develop a robust, yet simple, approach to overcoming chemical and photochemical instability. Avalanche breakdown of the Ge bottom cell enabled STH efficiencies that were larger than anticipated given light absorption by water. However, it is important to note that the photovoltaic device was not optimized for either terrestrial applications or use in water. While an STH efficiency of >10% was achieved in the present work, use of custom-designed tandem photovoltaic cells with bandgaps optimized by considering the real spectral irradiance in the operational environment would yield significant performance improvements. Ideally, such designs would consider not just transmission through the electrolyte, but also optical filtering by the polymer component of the composite protection layer, as well as potential benefits of integrated anti-reflection coatings.

The stability of several key interfaces requires careful management. The cleaning and surface preparation processes described in the Methods section were developed to ensure good coating uniformity and adhesion between the PV, wire mesh, and epoxy. This was essential for preventing penetration of electrolyte into the assembly, which would result in rapid chemical attack of the triple junction cell and device failure. However, as noted above, gradual degradation of device performance was observed after 5 days of testing under simulated diurnal cycling. It was determined that the origin of this photocurrent decline was loss of catalyst from the grid surface, likely as a consequence of stress corrosion cracking. Deposition of thin metallic adhesive interlayers, control of catalyst film microstructure and stress, and elimination of interfacial oxides susceptible to penetration by electrolyte are all possible routes to avoiding catalyst loss by this mechanism and improving durability.

Nucleation and growth of large, anchored bubbles was commonly found during these experiments (see Supporting Videos). This indicates that the unstirred

electrolyte/device interface was unfavorable for rapid detachment of small bubbles. The presence of bubbles results in light scattering that can affect the intensity and wavelength distribution of light available to be absorbed. Furthermore, their presence reduces the solid/liquid contact area, thereby reducing the concentration of available catalytic centers. Careful management of surface energies using stable chemistries may help promote bubble detachment from surfaces, which would improve the time-averaged product generation rate.

The usefulness of the architecture described here depends not only on these paths to improvement but also on amenability to scaling to surface areas of practical size. In this work, the PV element was kept to 1 cm^2, but there do not appear to be serious limitations to using the same approach to fabricate much larger devices. This is in contrast to other corrosion protection approaches that are dependent on the controlled deposition of thin films, often using energy-intensive vacuum processing. Extension of those approaches to larger scales will require migration to larger tooling and development of new processes to manage film homogeneity and defects in these complex materials systems. The potential for facile scaling of the composite protection strategy presented here represents an important advantage in the quest for practical solar water splitting devices and, ultimately, solar fuels generators.

4. Conclusion

In this work, we demonstrated a new strategy for creating stable and efficient solar water splitting devices. This advance was based on a composite coating comprising a catalyst-coated metallic grid embedded in a transparent polymer, which allowed chemically sensitive semiconductors to be protected from the harsh reaction environments associated with photoelectrolysis, while also allowing charge transport between light absorber and catalyst layers. We showed that application of this coating to a triple junction photovoltaic stack and assembly in a membrane-integrated device

yielded a solar-to-hydrogen conversion efficiency of >10% with full gas product separation in both acid and base, under either continuous illumination or diurnal light cycling, both indoors and outdoors. Stability of the device extended to operational times longer than four days, with subsequent efficiency reductions associated with catalyst loss rather than chemical corrosion of the semiconductors. Taken together, these characteristics classify this device as a safe and integrated solar hydrogen generator that is robustly protected against corrosion. The protective coating does not require energy-intensive processing steps, eliminates potential material and thermal processing incompatibilities between different components, and could be feasibly manufactured at large scale. Furthermore, the approach is versatile and could be rapidly re-configured for use with a range of semiconductors, catalysts, and device architectures. Analysis of the functional characteristics of individual device components, as well as performance evaluation of the assembled system, revealed specific opportunities for improvements in device processing and design that are expected to lead to significant increases in both efficiency and stability.

5. Experimental Section

Chemicals: Unless otherwise noted, all chemicals were used as-received. Aqueous electrolyte solutions were all prepared using deionized water, with a resistivity of >18.2 MΩ-cm, from a Millipore water system. The 1 M H_2SO_4 electrolyte was prepared by dilution of ACS reagent grade, 95.0-98.0% H_2SO_4 (Sigma Aldrich). The 1 M KOH electrolyte was prepared by dissolution of technical grade, 45% w/w KOH (BDH, VWR). The composite coating was formed using commercial Epotek 302-3M epoxy (Epoxy Technologies, Billerica, MA).

Photovoltaic elements: The photovoltaic element, which forms the core of the monolithically integrated device demonstrated here, was a commercially available Ultra Triple Junction (UTJ) cell from Spectrolab, Inc. Although the purchased cell was designed for non-terrestrial applications under AM0 irradiance, its output characteristics make it well suited for solar

water splitting at >10% STH efficiency, as described in the main text. The as-received cells (active area 26.62 cm^2) were diced into 1×1 cm^2 pieces. After dicing, the material was cleaned in a heated xylene bath at 50 °C, rinsed with isopropanol, then dried under flowing high purity N$_2$. We note that no edge passivation was applied, which leads to some reduction of power conversion efficiency relative to the as-received cell.

Chassis: The chassis is shown schematically in Figure 3 and served to fix the geometric positons of all device components, including light absorber, catalysts, membrane, and electrolyte. Dimensions were selected based on outputs of computational device modelling, and its component pieces were machined from acrylic. After machining, the parts were cleaned in mildly agitated deionized water containing detergent for 10 - 20 min, after which they were rinsed in cold deionized water. A deionized water stream was used to clean out screw holes and ports. Next all parts were again rinsed in cold deionized water, rinsed with warm deionized water, and dried under flowing N$_2$.

Quartz windows (GM Associates, Oakland, CA) were epoxied into position using Epo-Tek 302-3M (Epoxy Technologies, Billerica, MA) and cured at 60 °C for 12 h. Inlet and outlet ports, formed from Upchurch PEEK tubing with an outer diameter of 1.8 mm and an inner diameter of 1.05 mm, were also epoxied in place using Epo-Tek 302-3M. Viton 75 O-rings (McMaster Carr) were used to seal each of the chambers. The two chambers, chip carrier, and membrane were compressed together using stainless steel socket head cap head bolts (size 2-56 length 0.50 inch).

Membranes: For the alkaline experiments an AHA-type Neosepta anion exchange membrane was used. Prior to use, the Neosepta membrane was rinsed with 1 M KOH and stored in 1 M KOH for 24 hours. For the acidic experiments, Nafion XL-100 was soaked in milli-Q water for 1 h before use.

Grid and Catalyst Preparation: Titanium grids were purchased from BeanTown Chemical and consisted of 0.28 mm diameter wire woven into an 18 wire per inch mesh. The as-received grids were solvent-cleaned by sequential sonication in acetone (BDH, semiconductor grade) and isopropanol (BDH, semiconductor grade), followed by drying under high purity N_2. Grids were then immediately loaded into a Kurt J. Lesker 5-gun confocal sputtering system with a base pressure of 7×10^{-7} Torr for catalyst deposition. The chamber was equipped with a Ti (99.995%) target, obtained from Kurt J. Lesker (Livermore, CA), as well as Pt (99.99%) and Ir (99.9%) targets made in-house at Lawrence Berkeley National Laboratory. For driving the hydrogen evolution reaction, Pt was selected as the catalyst and was deposited by radio frequency (rf) sputtering. Prior to sputter deposition, the substrates were cleaned by sputter etching at 25 W for 3 min in an Ar plasma at 5 mTorr. Immediately after this treatment, a 10 nm Ti adhesion layer was deposited onto the substrate by rf sputtering at 3.7 W cm^{-2} at a pressure of 2 mTorr in Ar. Finally, 100 nm of catalyst (Pt for HER or Ir for acidic OER) was deposited by rf sputtering in a 2mTorr atmosphere of Ar, also at 3.7 W cm^{-2}. For alkaline OER catalysis, NiFe was deposited by co-sputtering Ni and Fe to give a 50:50 atomic ratio. The sputtering sequences included a 1 min overlap between Ti and catalyst deposition steps. These processes were repeated on the opposite sides of the meshes. All materials were sputtered at room temperature, and the deposition rates were determined using a quartz crystal monitor.

The epoxy was prepared by weighing the two components to a weight ratio of 100:45, following by manual mixing for 1 min. Next, the epoxy was degassed in chamber evacuated to 150 mTorr for 5 min, after which it was purged with nitrogen. To create the composite coating, the catalyst-coated wire grid was mechanically pressed against the surface of the photovoltaic element with a custom 2-point compression unit held in place with finger-tightened nuts on threaded support rods.

22

The epoxy was then applied to the grid/photovoltaic assembly and cured in at 55 C for 12 h in air, after which it was cooled to room temperature.

Materials Characterization: The optical transmission of the various materials was measured using a Shimadzu SolidSpec-3700 UV-VIS-NIR spectrophotometer. All optical measurements were conducted with freshly prepared samples in ambient lab environment. Electron micrographs were captured using a FEI Quanta FEG 250 system at an electron acceleration voltage of 10 keV and elemental mapping was performed using a Bruker Quantax energy dispersive X-ray detector.

Electrochemical and Photoelectrochemical Measurements: The pH values of all aqueous solutions were measured using a Thermo Scientific Orion Dual Star meter with a Orion 8102BNUWP Ross Ultra Combination pH probe, yielding pH 13.7 for the 1 M KOH and pH 0 for 1 M H_2SO_4. All electrochemical, photoelectrochemical, and solid state photovoltaic data were collected using a Biologic SP-300 potentiostat. For two electrode measurements, the reference and counter electrode leads were electrically connected; for (photo)electrochemical measurements, these leads were connected to the OER catalyst and for solid state PV measurements these were connected to the dark backside contact of the device. Three electrode (photo)electrochemical measurements were conducted using a leak-free Ag/AgCl reference electrode (Innovative Instruments, Inc.) and a Pt wire counter electrode.

For indoor photoelectrochemical measurements, simulated sunlight was produced using a AAA-rated Newport Oriel Sol3A equipped with a Xe lamp and AM 1.5 G filter to obtain a 12 in. × 12 in. illumination area. A Newport 91150V reference cell with a calibrated monocrystalline silicon solar cell and an integrated thermocouple was used to measure the solar irradiance. The reference cell was calibrated and traceable to both NREL and to the International System of Units (SI). Solar water splitting devices were positioned to receive 1 sun illumination at the front window surface, as determined

using the reference cell. Water filtration experiments were performed using quartz cuvettes with path lengths through the water of 10 mm or 20 mm. Since the quartz cuvette area was larger than the PV element, an aperture was positioned between it and the PV to reduce light concentration effects. Video footage of devices under test was captured using a Microsoft Lifecam. During outdoor testing, the reference cell was positioned on the 2-axis solar tracker in the same plane as the solar water splitting device to monitor irradiance.

Just prior to starting the PEC measurement the photoelectrode assembly was exposed to an oxygen plasma (Plasma Preen II-973 Reactor) at full power for 1 min, with a 3 sccm flow of oxygen, and with a faraday cage covering the sample. This treatment reduced the water contact angle and bubble accumulation during device operation.

Gas production from the illuminated cathode chamber and dark anode chamber were monitored using two inverted burettes connected to digital monometers to measure the change in pressure as the water volume was displaced by gas in the head space of each burette. The measured gas production rates were converted to electrical currents using Faraday's law of electrolysis, combined with the ideal gas law. In particular, 1 mA of electrical current is equivalent of 0.44 mL h^{-1} of H_2 generation and 0.22 mL h^{-1} of O_2 generation at room temperature (25 °C). A small correction (typically 2-3%) was also applied to each data point to compensate for the pressure differential caused by the water level (typically 20-30 cm high) in each burette. The relationship between the current and the gas-production rate was verified experimentally using a water-splitting electrolyzer, and the calibration was performed regularly to confirm the continued accuracy of the relationship. The gas-production rates from the cathode and anode compartments generally maintained a ratio close to 2:1.

Gas chromatography (GC) was utilized to analyze production and compositions of gases. The GC (Agilent, 7890A Santa Clara, CA) was equipped with two-channels, between which measurements could be toggled. One of the set of columns was optimized for hydrogen detection with Ar as the carrier gas and the other set of columns was optimized for O_2 and N_2 detection, with He as the carrier gas. The cycle time for each GC run was 7 min. Calibration curves for H_2 and O_2 were obtained with a 3-point calibration curve at 100, 1000, and 9918 ppm and 100, 1000, and 8000 ppm, respectively. Prior to calibration, the system was purged for 10 min with 10 sccm of the calibration gas of interest, after which the mass flow controllers were set to 2 sccm. A minimum of 10 samples were collected for each calibration point.

During the gas composition analysis experiments, the device and GC were connected inline, with N_2 flowing through the anode and cathode chambers of the device and then to the sample loops of the GC. A flow rate of 2 sccm was used to ensure products were continually swept from the device. Prior to starting the GC experiment, the anode and cathode chamber were purged with 2 sccm of N_2 for 10 min. During both calibration and PEC experiments, the mass flow controller and meter (Alicat Scientific, 10 sccm full scale) were continually monitored for deviation from 2 sccm, as this could indicate leaks in the system or other errors in the measurement. The mass flowrate was based on the MW of the balance gas.

Supporting Information
Supporting Information is available from the Wiley Online Library or from the author.

References

[1]   A. Fujishima, K. Honda, Nature **1972**, 238, 37.

[2]   J. W. Ager, M. R. Shaner, K. A. Walczak, I. D. Sharp, S. Ardo, Energy Environ. Sci. **2015**, 8, 2811.

[3]   M. M. May, H.-J. Lewerenz, D. Lackner, F. Dimroth, T. Hannappel, Nature Comm. **2015**, 6, 8286.

[4]   E. Verlage, S. Hu, R. Liu, R. J. R. Jones, K. Sun, C. Xiang, N. S. Lewis, H. A. Atwater, Energy Environ. Sci. **2015**, 8, 3166.

[5]   J. Luo, D. A. Vermaas, D. Bi, A. Hagfeldt, W. A. Smith, M. Grätzel, Adv. Energy Mater. **2016**, 6, 1600100.

[6]   M. R. Shaner, H. A. Atwater, N. S. Lewis, E. W. McFarland, Energy Environ. Sci. **2016**, 9, 2354.

[7]   R. Sathre, C. D. Scown, W. R. Morrow, J. C. Stevens, I. D. Sharp, J. W. Ager, K. Walczak, F. A. Houle, J. B. Greenblatt, Energy Environ. Sci. **2014**, 7, 3264.

[8]   R. Sathre, J. B. Greenblatt, K. Walczak, I. D. Sharp, J. C. Stevens, J. W. Ager, F. A. Houle, Energy Environ. Sci. **2016**, 9, 803.

[9]   C. A. Rodriguez, M. A. Modestino, D. Psaltis, C. Moser, Energy Environ. Sci. **2014**, 7, 3828; B. A. Pinaud, J. D. Benck, L. C. Seitz, A. J. Forman, Z. B. Chen, T. G. Deutsch, B. D. James, K. N. Baum, G. N. Baum, S. Ardo, H. L. Wang, E. Miller, T. F. Jaramillo, Energy Environ. Sci. **2013**, 6, 1983.

[10]   S. Haussener, C. X. Xiang, J. M. Spurgeon, S. Ardo, N. S. Lewis, A. Z. Weber, Energy Environ. Sci. **2012**, 5, 9922.

[11]   S. Haussener, S. Hu, C. Xiang, A. Z. Weber, N. S. Lewis, Energy Environ. Sci. **2013**, 6, 3605; M. A. Modestino, C. A. Diaz-Botia, S. Haussener, R. Gomez-Sjoberg, J. W. Ager, R.

A. Segalman, Phys. Chem. Chem. Phys. **2013**, 15, 7050; A. Berger, R. Segalman, J. Newman, Energy Environ. Sci. **2014**, 7, 1468; J. Newman, J. Electrochem. Soc. **2013**, 160, F309.

[12]   S. Chen, L.-W. Wang, Chem. Mater. **2012**, 24, 3659.

[13]   S. Hu, N. S. Lewis, J. W. Ager, J. Yang, J. R. McKone, N. C. Strandwitz, J. Phys. Chem. C **2015**, 119, 24201; A. G. Scheuermann, P. C. McIntyre, J. Phys. Chem. Lett. **2016**, 7, 2867; R. Liu, Z. Zheng, J. Spurgeon, X. Yang, Energy Environ. Sci. **2014**, 7, 2504; A. Paracchino, V. Laporte, K. Sivula, M. Graetzel, E. Thimsen, Nature Mater. **2011**, 10, 456; Y.W. Chen, J.D. Prange, S. Duehnen, Y. Park, M. Gunji, C.E.D. Chidsey, P.C. McIntyre, Nature Mater. **2011**, 10, 539; M. Haro, C. Solis, G. Molina, L. Otero, J. Bisquert, S. Gimenez, A. Guerrero, J. Phys. Chem. C, **2015**, 119, 6488; H. Kumagai, T. Minegishi, N. Sato, T. Yamada, J. Kubota, K. Domen, J. Mater. Chem. A, **2015**, 3, 8300.

[14]   K. Sun, M. T. McDowell, A. C. Nielander, S. Hu, M. R. Shaner, F. Yang, B. S. Brunschwig, N. S. Lewis, J. Phys. Chem. Lett. **2015**, 6, 592.

[15]   J. Yang, K. Walczak, E. Anzenberg, F. M. Toma, G. Yuan, J. Beeman, A. Schwartzberg, Y. Lin, M. Hettick, A. Javey, J. Am. Chem. Soc. **2014**, 136, 6191; X. Zhou, R. Liu, K. Sun, K. M. Papadantonakis, B. S. Brunschwig, N. S. Lewis, Energy Environ. Sci. **2016**, 9, 892; J. Yang, J. K. Cooper, F. M. Toma, K. A. Walczak, M. Favaro, J. W. Beeman, L. H. Hess, C. Wang, C. Zhu, S. Gul, J. Yano, C. Kisielowski, A. Schwartzberg, I. D. Sharp, Nature Mater. **2016**, advance online publication.

[16]   K. Sun, R. Liu, Y. Chen, E. Verlage, N. S. Lewis, C. Xiang, Adv. Energy Mater. **2016**, 6, 1600379.

[17]   S. Y. Chen, L. W. Wang, Chem. Mater. **2012**, 24, 3659; F. M. Toma, J. K. Cooper, V. Kunzelmann, M. T. McDowell, J. Yu, D. M. Larson, N. J. Borys, C. Abelyan, J. W. Beeman, K. M. Yu, J. Yang, L. Chen, M. R. Shaner, F. A. Houle, K. A. Persson, I. D. Sharp, Nature Comm. **2016**, 7, 12012.

[18]   H. Cotal, C. Fetzer, J. Boisvert, G. Kinsey, R. King, P. Hebert, H. Yoon, N. Karam, Energy Environ. Sci. **2009**, 2, 174.

[19]   Azur Space Solar Power GMBH, 2012-11-30; Spectrolab, 2010-05-10.

[20]   J. Jin, K. Walczak, M. R. Singh, C. Karp, N. S. Lewis, C. Xiang, Energy Environ. Sci. **2014**, 7, 3371.

[21]   S. A. Bonke, M. Wiechen, D. R. MacFarlane, L. Spiccia, Energy Environ. Sci. **2015**, 8, 2791.

[22]   H. Doscher, J. F. Geisz, T. G. Deutsch, J. A. Turner, Energy Environ. Sci. **2014**, 7, 2951.

[23]   M. A. Steiner, J. F. Geisz, Appl. Phys. Lett. **2012**, 100, 251106.

[24]   G. Segev, G. Mittelman, A. Kribus, Solar Energy Materials & Solar Cells **2012**, 98, 57.

[25]   A. Ben Or, J. Appelbaum, Progress in Photovoltaics: Research and Applications 2013, 21, 713; H. Kawamura, K. Naka, N. Yonekura, S. Yamanaka, H. Kawamura, H. Ohno, K. Naito, Solar Energy Materials and Solar Cells 2003, 75, 613.

[26]   Z. Chen, T. F. Jaramillo, T. G. Deutsch, A. Kleiman-Shwarsctein, A. J. Forman, N. Gaillard, R. Garland, K. Takanabe, C. Heske, M. Sunkara, Journal of Materials Research 2010, 25, 3.

Figures
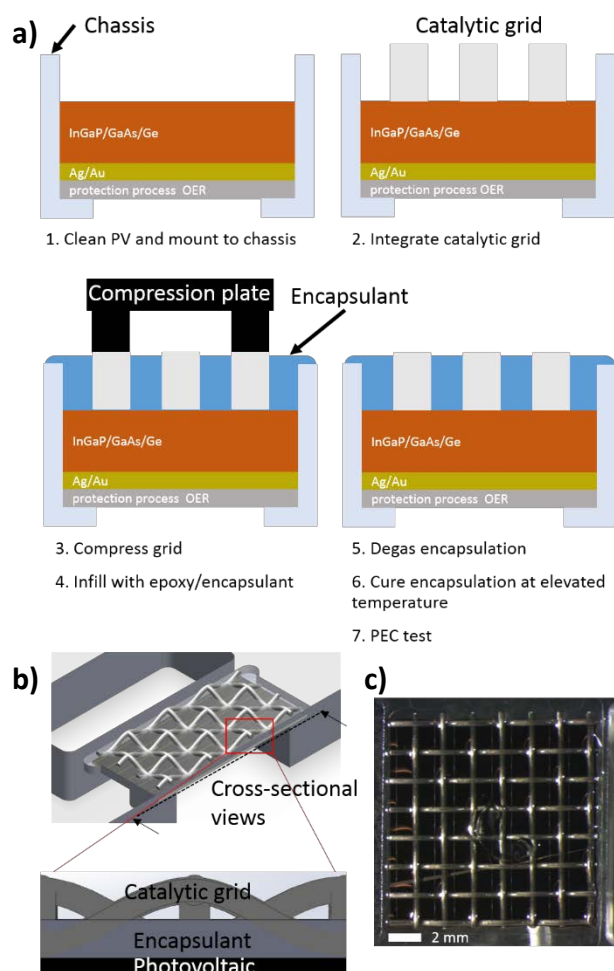
Figure 1. Integration of the composite protection coating with the photovoltaic element. a) Process flow for forming the catalytic composite protection layer directly on the surface of the photovoltaic (PV) element. b) Cross-sectional illustration of the photoelectrode assembly, showing the protrusion of the catalytic grid out of the epoxy encapsulant, where it can make contact with electrolyte. c) Top-down photograph of an assembled triple junction solar cell with the catalytic composite protective layer on its surface. The scale bar is 2 mm.
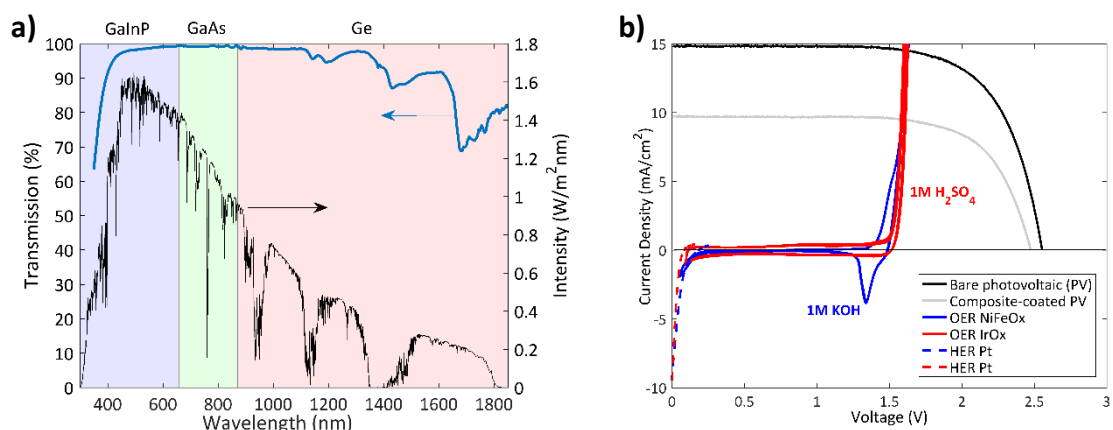
Figure 2. a) The measured optical transmission of the epoxy component of the composite coating (blue line) is shown as a function of wavelength and compared to the AM1.5G solar spectrum (black line). The Ti mesh had a uniform transmission of 67.4% across the measured wavelengths (not shown). The colored regions indicate the spectral ranges absorbed by each of the junctions of the photovoltaic element. b) Comparison of the OER (solid red and solid blue curves) and HER (dashed red and dashed blue curves) electrocatalyst activity in a three-electrode configuration in 1 M H_2SO_4 (red solid and dashed curves) and 1 M KOH (blue solid and dashed curves), overlaid with the solid state solar cell performance without (black) and with (grey) the composite coating. A common *x*-axis scale between the electrochemical and solid state electrical measurements was established by setting the voltage to reach a current density of -8.13 mA/cm^2 (approximating the current density to reach 10% STH efficiency) from the Pt HER catalysts as the zero point.
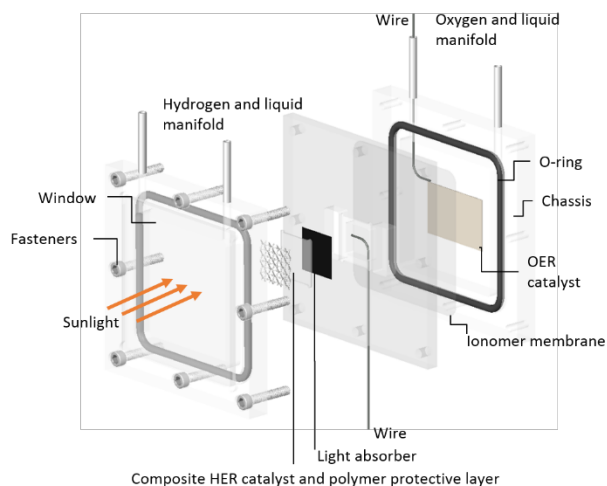
Figure 3. Expanded schematic illustration of the solar water splitting device and chassis. The anode and cathode chambers are separated by an ionomer membrane that extends across two channels on either side of the mounted photovoltaic device. Details of the materials used for each element are presented in Table 1.

Table 1 Solar water splitting device components used under acidic and alkaline conditions.

Type	Electrolyte	Light Absorber/PV	HER Catalyst	OER Catalyst	Membrane	Catalyst Support/ Anticorrosion Layer
Acid	1 M H_2SO_4 (aq)	Spectrolabs UTJ	Pt	IrOx	Nafion XL-100	Ti 30 mesh in Epo-Tek 302-3M
Base	1 M KOH (aq)	Spectrolabs UTJ	Pt	NiFeOx	AHA Neosepta	Ti 30 mesh in Epo-Tek 302-3M
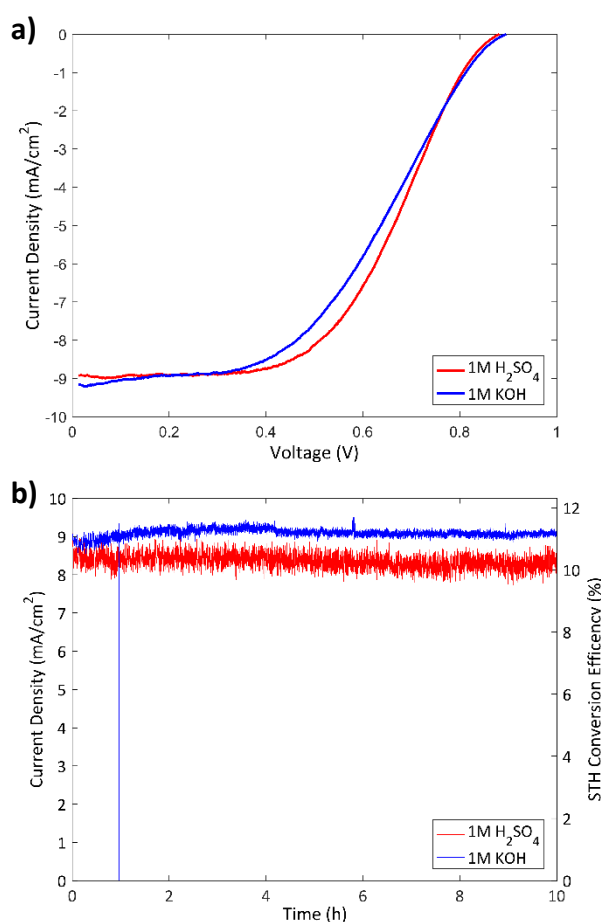
Figure 4. a) Two-electrode cyclic voltammograms from the same composite-protected device operated in 1 M KOH with IrO_x OER catalyst (blue) and 1 M H_2SO_4 with $NiFeO_x$ OER catalyst (red). b) Chronoamperometric characterization of the same device with no applied bias and operated for 10 h under 1 M KOH (blue) and 1 M H_2SO_4 (red). The solar-to-hydrogen conversion efficiency presented on the right axis was calculated according to Equation 1. The same protected photovoltaic element was used for all of these tests, but the membrane and OER catalyst were changed for operation under acidic and alkaline environments, as summarized in Table 1.

Table 2 Tabulated solar-to-hydrogen efficiencies, along with gas compositions in cathode and anode chambers measured by gas chromatography, from the same device operated in 1 M KOH and 1 M H_2SO_4.

Electrolyte	STH conversion efficiency (%)	H_2 crossover anode (%)	O_2 crossover cathode (%)	H_2/O_2
1 M KOH	10.90 +/- 0.09	1.37 +/- 0.073	0.12 +/- 0.43	2.17 +/- 0.007

| 1 M H$_2$SO$_4$	10.54 +/- 0.24	0.94 +/- 0.123	0.37 +/- 1.53	2.38 +/- 0.040
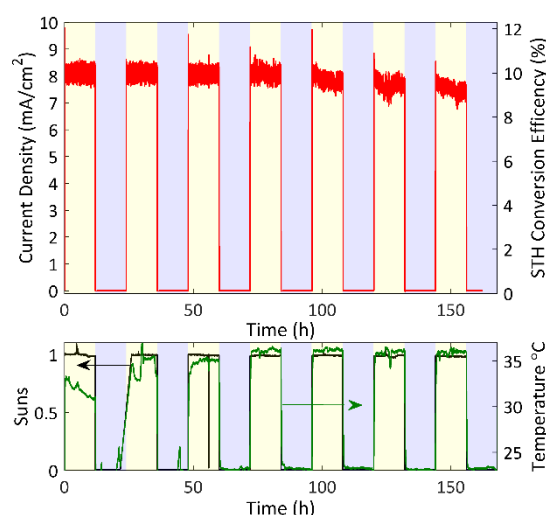
Figure 5. (top panel) Composite-protected solar water splitting device performance measured over 7 days of simulated diurnal cycling with 12 h intervals of illumination (1 sun AM 1.5G) and darkness with no applied bias, operated in 1 M H$_2$SO$_4$ with IrO$_x$ OER catalyst. The left axis shows the recorded photocurrent and the right axis shows the corresponding solar-to-hydrogen conversion efficiency calculated according to Equation 1, both as a function of time. (bottom panel) The illumination intensity (black), reported as number of suns, and temperature (greed) from a reference cell measured side-by-side with the solar water splitting device during the 7 day testing period.
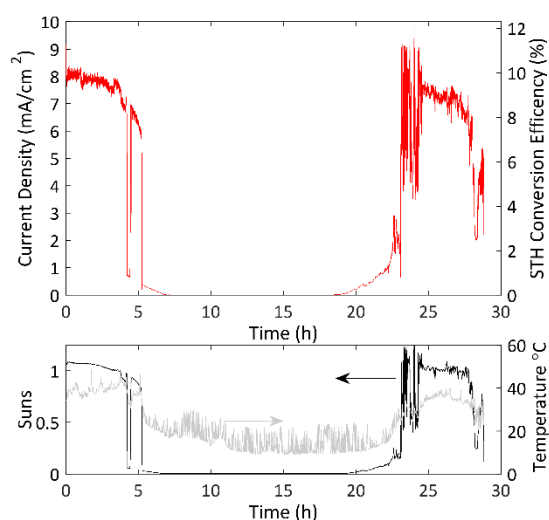

Figure 6. (top panel) Composite-protected solar water splitting device performance measured over 30 h of outdoor testing with no applied bias, operated in 1 M H$_2$SO$_4$ with IrO$_x$ OER catalyst. The left axis shows the recorded photocurrent and the right axis shows the corresponding solar-to-hydrogen conversion efficiency calculated according to Equation 1 and assuming a constant spectral distribution, both as a function of time. (bottom panel) The illumination intensity (black), reported as number of suns, and temperature (grey) from a reference cell measured side-by-side with the solar water splitting device during the 30 h

outdoor testing period. The illumination intensity recorded by the calibrated reference cell was used for calculation of the solar-to-hydrogen conversion efficiency in the top panel.
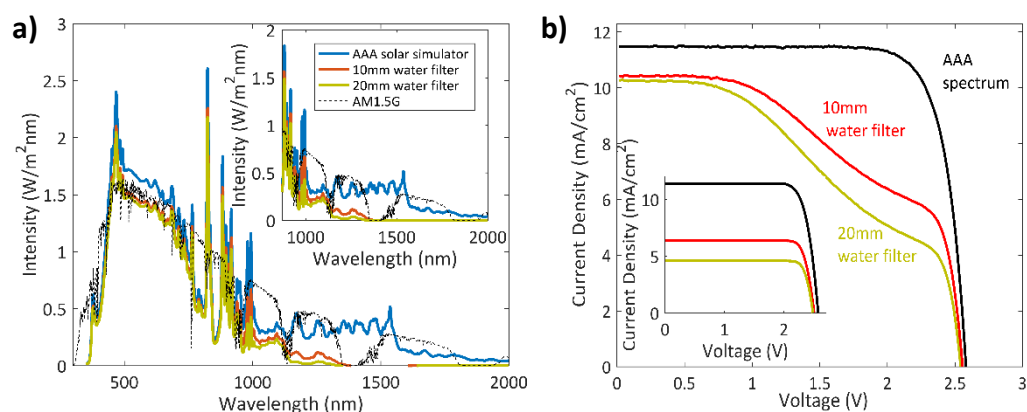
Figure 7. (a) The measured AAA solar simulator spectrum (blue) and the spectra obtained after transmission through the 10 mm (red) and 20 mm (orange) water filters. The AM 1.5G solar spectrum (black) is shown for comparison. The inset shows a zoom into the infrared portion of the solar spectrum, where optical absorption by water is strongest and leads to significantly reduced optical excitation of the Ge bottom cell of the photovoltaic element. (b) *JV* curves of diced UTJ cells illuminated with the unfiltered AAA solar simulator spectrum (black dashed), as well as with the 10 mm (red) and 20 mm (brown) thick water filters in place. The inset shows the same curves for simulated cells under the same conditions without including the Ge junction breakdown.
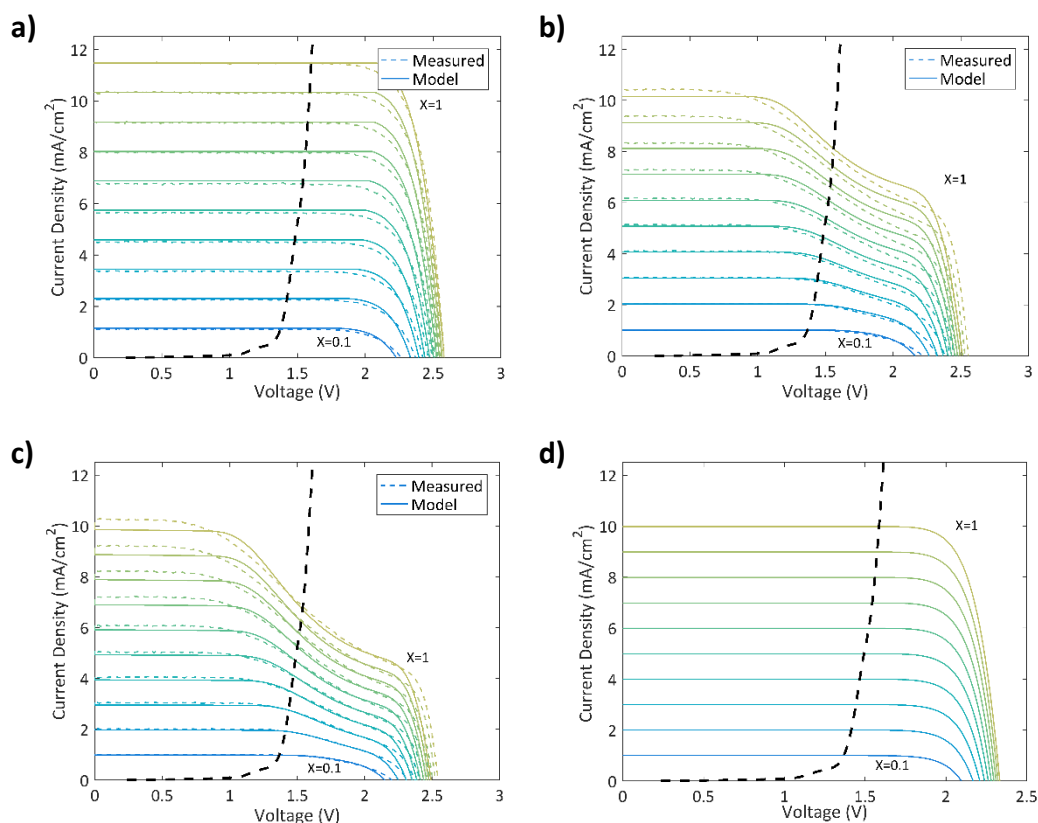
Figure 8. (a) Measured (dashed lines) and modelled (solid lines) JV curves from the triple junction photovoltaic element at different light intensities (x) between 0.1 and 1 Sun of the AAA solar simulator spectrum (a), with a 10 mm water filter in place (b), a 20mm water filter in place (c), and the modelled dual junction InGaP/GaAs cell assuming a 10 mm water filter (d). Solid state photovoltaic curves were obtained with the sample in air, following the relevant water filter. The black dashed line is the 2 electrode electrochemical load curve for the case of operation of Pt HER and IrO$_x$ OER catalysts in 1 M H$_2$SO$_4$ and its intersection with the photovoltaic JV curves defines the operating point for the unbiased device.
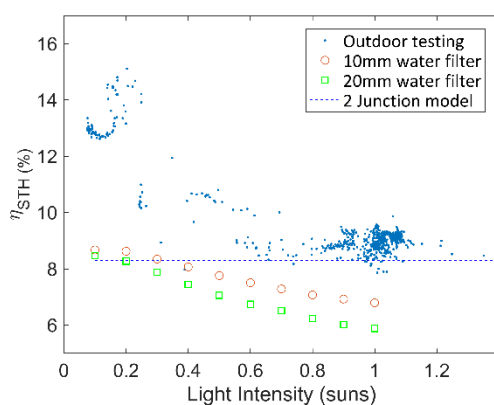

Figure 9. Solar-to-hydrogen conversion efficiency versus light intensity from the outdoor testing reported in Figure 6. The trend of increasing conversion efficiency with decreasing light intensity is in agreement with the trends from model results for illumination through 10 mm and 20 mm water filters and the Ti mesh, presented as the open symbols. This trend is a consequence of the Ge junction breakdown, as described in the text. The horizontal dashed line represents the predicted performance from a hypothetical dual junction device in Figure 8d, where conversion efficiency is light intensity independent.

A novel composite coating enables stable and efficient solar hydrogen generation under both basic and alkaline conditions and provides a versatile approach to scalably protecting semiconductor light absorbers, integrating catalysts, and managing charge transport. This strategy is verified by demonstration of devices with unbiased solar-to-hydrogen conversion efficiencies exceeding 10% with pure gas product streams in both laboratory and outdoor testing environments.

Karl A. Walczak, Gideon Segev, David M. Larson, Jeffrey W. Beeman, Frances A. Houle, Ian D. Sharp*

Hybrid Composite Coatings for Durable and Efficient Solar Hydrogen Generation Under Diverse Operating Conditions

WILEY-VCH
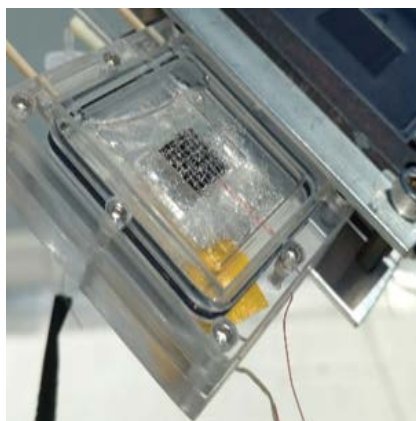
Supporting Information

## Hybrid Composite Coatings for Durable and Efficient Solar Hydrogen Generation Under Diverse Operating Conditions

Karl A. Walczak, Gideon Segev, David M. Larson, Jeffrey W. Beeman, Frances A. Houle, Ian D. Sharp*

**Table S1.** Solar driven water splitting demonstrations with III-V multi-junction photovoltaics in reverse chronological order.

| Publication	Device Structure PV and Electrolyzer	Electrolyte and Illumination Conditions	STH Efficiency	Stability
Jia et al.[1] (2016)	InGaP/GaAs/GaInNAsSb monolithic PV in air 2x series connected MEA	Water Anolyte 42 Suns	Average = 28%	48 hours constant current density
Sun et al.[2] (2016)	GaAs/InGaP/TiO$_2$ monolithic PV in electrolyte integrated Ni OER catalyst wired CoP HER catalyst bipolar membrane	Catholyte 1 M H$_2$SO$_4$ Anolyte 0.5 M KBi (pH 9.3) 100 mW cm^{-2}	10%	100 hours constant current
Verlage et al. [3] (2015)	GaAs/InGaP/TiO$_2$ monolithic PV in electrolyte integrated Ni OER catalyst wired CoP HER catalyst AEM membrane	1 M KOH 100 mW cm^{-2}	10%	40 hours constant current
Nakamura et al [4] (2015)	GaInP/GaAs/Ge 5x monolithic PV in air 3x series connected MEA	Water 761.2 W m^2	24.4%	10 minutes outdoor testing
Bonke et al. [5] (2015)	GaInP/GaAs/Ge monolithic PV in air wired Ni foam OER catalyst wired Ni foam HER catalyst	1 M H$_2$SO$_4$ 0.6 M Bi + Na$_2$SO$_4$ (pH 9.3) 1 M NaOH 100 Suns	22%	24 hours constant current 72 hour cycling 12 hours light on and off
May et al [6] (2015)	GaInP/GaInAs monolithic PV in electrolyte integrated RuO$_x$ OER catalyst integrated Rh HER catalyst	pH 0 1 M HClO$_4$ 100 mW cm^2	14%	150 seconds constant current
Modestino et al.[7]. (2014)	GaInP$_2$(pn)/GaAs(pn)/Ge(pn) 3J monolithic PV in air wired Pt HER catalyst wired Pt OER catalyst Nafion membrane	pH 9.2 electrolyte recirculation 100 mW cm^{-2}	6.2%	15 hours constant current density

Fujii *et al.*[8] (2013)	GaInP(pn)/InGaAs(pn)/Ge(pn) 3J PV in air wired Pt HER catalyst wired Pt OER catalyst Nafion MEA	pH 7 10x optical concentration	15% (3 solar cells, two PEM electrolyzers), 12% (one PV, one PEM)	1 hour constant current and H_2 production
Peharz et al.[9] (2007)	$Ga_{0.83}In_{0.17}As$(pn)//$Ga_{0.35}In_{0.65}P$(pn) monolithic PV in air wired Pt HER catalyst wired IrO_2 OER catalyst Nafion MEA PV + electrolyzer	pH 7 membrane separated evolution of products 500x optical concentration	15%	2.3 hours stable current in outdoor test
Khaselev et al.[10] (2001)	$GaInP_2$(pn)//GaAs(pn) monolithic PV in air wired Pt HER catalyst integrated Pt OER catalyst	2 M KOH co-evolved products 100 mW cm^{-2}	16.5%	9 hours stable current in outdoor test
Licht et al.[11] (2000)	$Al_{0.15}Ga_{0.85}As$(pn)//Si(pn) monolithic PV in air integrated Pt HER catalyst integrated RuO_2 OER catalyst PV + electrolyzer	1 M $HClO_4$ co-evolved products 135 mW cm^{-2}	18.3%	14 hours stable photocurrent
Khaselev and Turner[12] (1998)	SLJ $GaInP_2$(p)//GaAs(pn) monolithic PV in electrolyte integrated Pt HER catalyst wired Pt OER catalyst Semiconductor liquid junction	3 M H_2SO_4, 0.01 M Triton X-100 co-evolved products 11 suns	12.4%	20 hours 20% drop in current
Kainthla *et al.*[13] (1987)	SLJ InP(p)//GaAs(n) SLJ cells wired side-by-side in electrolyte integrated Pt HER catalyst integrated MnO OER catalyst Semiconductor liquid junction	6M KOH	8.2%	10 hours initial 10% current drop
Mettee *et al.*[14] (1981)	SLJ GaP(p)//Fe_2O_3(n) SLJ wired PV in electrolyte wired Pt HER catalyst integrated RuO_2 OER catalyst Semiconductor liquid junction	1M Na_2SO_4 fritted compartments sunlight	0.02 – 0.1%	Not reported

Ohashi *et al.*[15] (1977)	SLJ CdTe(p)//TiO_2(n) SLJ
	SLJ GaP(p)//TiO_2(n) SLJ
	SLJ CdTe(p)//SrTiO3(n) SLJ
	SLJ GaP(p)//$SrTiO_3$(n) SLJ
	cells wired side-by-side
	Semiconductor liquid junction
		1 M NaOH
		co-evolved products
		100 mW cm^{-2}
			0.044%, 0.098%, 0.18%, 0.67%, respectively	1 hour stable photovoltage some cells tested to 50 hours

Nozik[16] (1976)	SLJ GaP(p)//TiO_2(n) SLJ wired PVs in air Semiconductor liquid junction	0.2 N H_2SO_4 co-evolved products 85 mW cm^{-2}	0.25%	Not reported

37
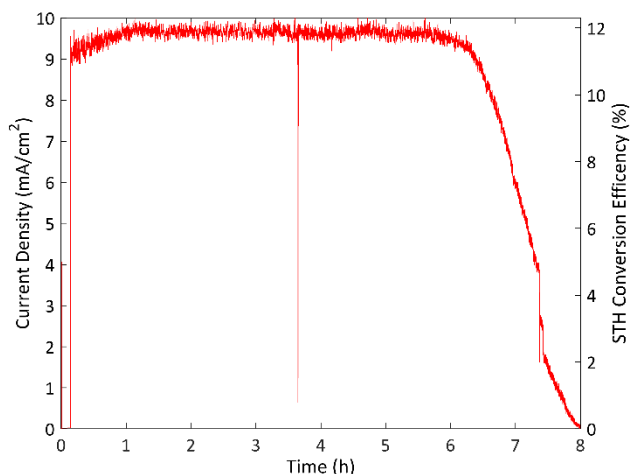
Figure S1. Representative chronoamperometric curve from a catastrophic failure of the photovoltaic element due to chemical attack, occurring at approximately 6.5 h. Such failure is characterized by a rapid decline of the photocurrent density and visible corrosion on the device. By comparison, performance degradation of the composite-protected device tested for 7 days (Figure 5) was gradual and attributed to catalyst loss from the metallic grid.
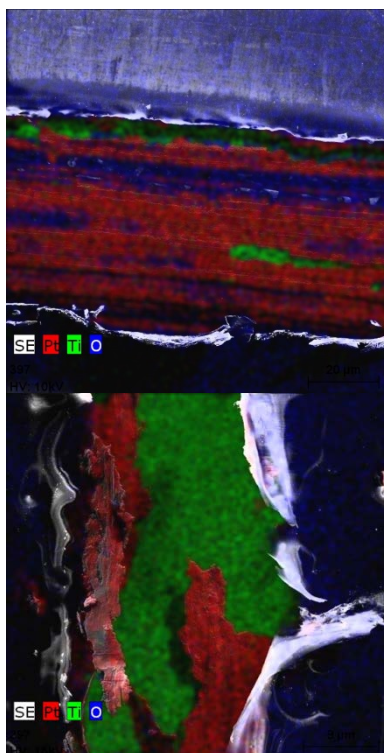
Figure S2. Scanning electron micrographs overlaid by elemental maps obtained via energy dispersive x-ray spectroscopy from Pt-coated Ti wire before (top) and after (bottom) 7 day operation with diurnal cycling (Figure 5). Delamination of the Pt catalyst during operation reveals the underlying Ti and gradually reduces the solar-to-hydrogen conversion efficiency.
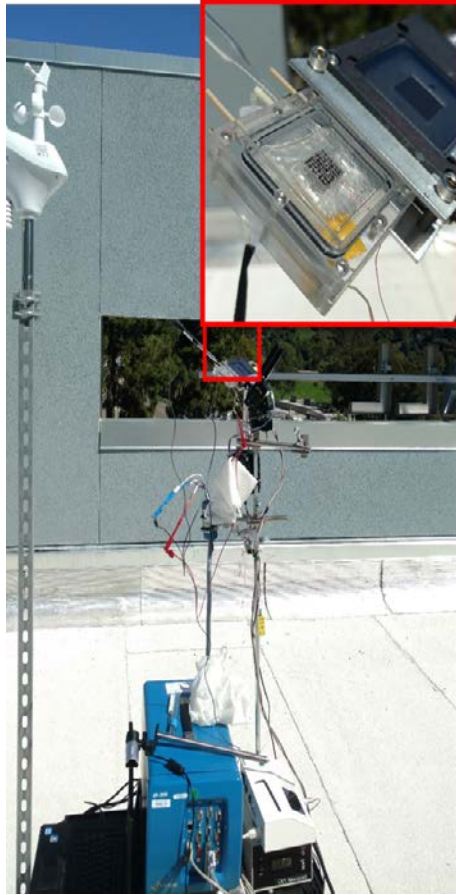
Figure S3. Photograph of the outdoor testing station, which includes a 2-axis solar tracker and analytical equipment, including a potentiostat for collecting the photocurrent as a function of time with no applied bias. The inset shows and close-up view of the device under test adjacent to the calibrated reference diode.

Device Modelling

The current mismatches caused by water-filtered illumination were investigated by fitting an equivalent circuit model to the device characteristics. The equivalent circuit consists of three photovoltaic sub-cells connected in series, each represented with a single diode equivalent circuit as described previously.[17] An illustration of the circuit is shown in Fig. S4. Subscripts 1-3 represent the top (InGaP), middle (GaAs), and bottom (Ge) sub-cells respectively. The photocurrent of each sub-cell was calculated by multiplying the external quantum efficiency curves supplied by the manufacturer by the incident photon flux and integrating the product:

$$J_{ph,i} = q \int_0^\infty EQE_i(\lambda) \cdot \Phi(\lambda) d\lambda$$

where q is the electron charge, EQE_i is the external quantum efficiency of the ith sub-cell, $\Phi(\lambda)$ is the incident spectrum, and λ is the wavelength. The current-voltage characteristics of the top and middle sub-cells follow:

$$V_i = \frac{n_i k_B T}{q} \ln\left(\frac{J_{ph,i} - J_L}{J_{0,i}} + 1\right)$$

where $J_{ph,i}$, $J_{o,i}$, J_L are the sub-cell photocurrent density, the diode reverse saturation current density, and the load current density, respectively. V_i is the voltage, n_i is the diode ideality factor (typically between 1 and 2), k_B is the Boltzmann constant, and T is the absolute temperature. The diode reverse saturation current follows:

$$J_{o,i} = \kappa_i \cdot T^{\left(3 + \frac{\gamma_i}{2}\right)} \exp\left(-\frac{E_{g,i}}{n_i k_B T}\right)$$

where E_g is the energy band gap and κ_i and γ_i are constants, where γ_i is typically between 0 and 2. In order to model the Ge junction performance under reverse bias, a breakdown term, J_{br}, was added to the equivalent circuit such that

$$J_L = J_{ph,3} - J_{o,3}\left(\exp\left(\frac{qV_3}{k_B T}\right) - 1\right) - J_{br}$$

and

$$J_{br} = \alpha \cdot V_3 \left(1 - \frac{V_3}{V_{br}}\right)^m$$

α and m are constants and V_{br} is the breakdown voltage.[18] The complete solar cell voltage is

$$V = \sum_{i=1}^{3} V_i - J_L \cdot A \cdot R_s$$

where A is the cell area and R_s is the total series resistance, including the resistances of the tunnel diodes, emitter layer, the contact grid, and the measurement apparatus. The model parameters where fitted to best match the *JV* curves under the solar simulator spectrum at intensities varying from 0.1 to 1 sun. The extracted equivalent circuit parameters can be found in Table S2.
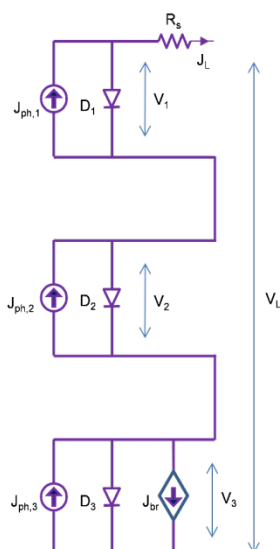
Figure S4. Triple junction photovoltaic cell equivalent circuit model, where subscripts 1-3 represent the top (InGaP), middle (GaAs), and bottom (Ge) sub-cells, respectively.

Table S2. Equivalent circuit parameters

Parameter	InGaP	GaAs	Ge
κ [mA/cm$^2\cdot$K^4]	$9.4\cdot10^{-9}$	$3.2\cdot10^{-2}$	$1.5\cdot10^{-3}$
n	1.99	1.99	1.98
γ	1.96	1.95	0.26
R_s (Ω)	4.8		
α [mA/cm$^2\cdot$V]	--	--	0.99
V_{br} (V)	--	--	-4.83
m	--	--	7.99

References

[1]   J. Jia, L. C. Seitz, J. D. Benck, Y. Huo, Y. Chen, J. W. D. Ng, T. Bilir, J. S. Harris, T. F. Jaramillo, Nature Commun. **2016**, 7, 13237.

[2]   K. Sun, R. Liu, Y. Chen, E. Verlage, N. S. Lewis, C. Xiang, Adv. Energy Mater. **2016**, 6, 1600379.

[3]   E. Verlage, S. Hu, R. Liu, R. J. Jones, K. Sun, C. Xiang, N. S. Lewis, H. A. Atwater, Energy Environ. Sci. **2015**, 8, 3166.

[4]   N. Akihiro, O. Yasuyuki, K. Kayo, H. Yoshihide, N. Kensuke, S. Masakazu, F. Katsushi, Appl. Phy. Express **2015**, 8, 107101.

[5]   S. A. Bonke, M. Wiechen, D. R. MacFarlane, L. Spiccia, Energy Environ. Sci. **2015**, 8, 2791.

[6]   M. M. May, H.-J. Lewerenz, D. Lackner, F. Dimroth, T. Hannappel, Nature Commun. **2015**, 6, 8286.

[7]   M. A. Modestino, K. A. Walczak, A. Berger, C. M. Evans, S. Haussener, C. Koval, J. S. Newman, J. W. Ager, R. A. Segalman, Energy Environ. Sci. **2014**, 7, 297.

[8]   K. Fujii, S. Nakamura, M. Sugiyama, K. Watanabe, B. Bagheri, Y. Nakano, Int. J. Hydrogen Energy **2013**, 38, 14424.

[9]   G. Peharz, F. Dimroth, U. Wittstadt, Int. J. Hydrogen Energy **2007**, 32, 3248.

[10]   O. Khaselev, A. Bansal, J. A. Turner, Int. J. Hydrogen Energy **2001**, 26, 127.

[11]   S. Licht, B. Wang, S. Mukerji, T. Soga, M. Umeno, H. Tributsch, J. Phys. Chem. B **2000**, 104, 8920.

[12]   O. Khaselev, J. A. Turner, Science **1998**, 280, 425.

[13]   R. C. Kainthla, B. Zelenay, J. O. M. Bockris, J. Electrochem. Soc. **1987**, 134, 841.

[14]   H. Mettee, J. W. Otvos, M. Calvin, Sol. Energy Mater. **1981**, 4, 443.

[15]   K. Ohashi, J. McCann, J. O. M. Bockris, Nature **1977**, 266, 610.

[16]   A. J. Nozik, Appl. Phys. Lett. **1976**, 29, 150.

[17]   G. Segev, G. Mittelman, A. Kribus, Solar Energy Materials and Solar Cells **2012**, 98, 57.

[18]   A. Ben Or, J. Appelbaum, Progress in Photovoltaics: Research and Applications **2013**, 21, 713.